PNAS RESEARCH ARTICLE | NEUROSCIENCE
PSYCHOLOGICAL AND COGNITIVE SCIENCES

Personalized functional topography–based multisite brain age prediction modeling reveals divergent neurodevelopment in major depression

Chenxuan Pang[a,b,c], Xiaoyi Sun[a,b,c,d], Jianlong Zhao[a,b,c], Xinyuan Liang[a,b,c], Lianglong Sun[a,b,c], Qixiang Lin[a,b,c], Jinrong Sun[e,f,g], Xiaowen Lu[e,f,h], Qiangli Dong[e,f,i], Liang Zhang[e,f,j], Xiaoqin Wang[k,l], Dongtao Wei[k,l], Yuan Chen[m], Bangshan Liu[e,f], Chu-Chung Huang[n], Yanting Zheng[o], Yankun Wu[p], Taolin Chen[q,r,s], Yuqi Cheng[t], Xiufeng Xu[u], Qiyong Gong[q,r,s], Tianmei Si[p], Shijun Qiu[o], Ching-Po Lin[v,w,x], Jingliang Cheng[m], Yanqing Tang[y], Fei Wang[y], Jiang Qiu[k,l], Peng Xie[z,aa], Lingjiang Li[e,f], Yong He[a,b,c,bb], DIDA-MDD Working Group[1], and Mingrui Xia[a,b,c,2]

Affiliations are included on p. 11.

Edited by Helen Mayberg, Icahn School of Medicine at Mount Sinai, New York, NY; received July 22, 2025; accepted February 10, 2026

Major depressive disorder (MDD) is associated with widespread alterations in functional brain networks across the lifespan. However, heterogeneity in atypical brain development among patients with MDD remains largely uncharacterized. Using a multisite resting-state functional MRI dataset consisting of 1,105 MDD patients and 1,065 healthy controls, we constructed a harmonized multicenter brain age prediction model based on individualized functional topography and identified two patient subgroups with positive or negative brain age gaps (BAGs). In patients with a positive BAG (BAG+), expansion of the salience network (SAL) into the dorsolateral prefrontal and ventrolateral prefrontal cortices, in addition to contraction of the sensorimotor and dorsal attention networks (DAN), contributes to accelerated brain aging. Conversely, in the negative BAG (BAG–) group, SAL expansion into the orbitofrontal cortex (OFC) and contraction of the visual and sensorimotor networks (SMN) were linked to delayed brain development. These subgroups also exhibited distinct neurodevelopmental trajectories. Clinically, BAG+ patients showed stronger associations between higher-order network topography and mood symptoms, whereas BAG– patients exhibited links between visual/default mode network topography and insomnia. At the molecular level, both groups showed enrichment of genes related to synaptic signaling but displayed distinct expression patterns and divergent expression trajectories in key neurodevelopmental gene sets. Notably, antidepressant treatment modulated the brain in ways that were specific to each subgroup. These findings reveal heterogeneous neurodevelopmental profiles in MDD with distinct biological and clinical signatures, offering insights into personalized precision medicine for this disorder.

major depressive disorder | brain age | lifespan trajectory | connectome | transcriptome

Significance

Major depressive disorder (MDD), with an onset from adolescence through adulthood, involves disruptions in the brain network with substantial neurobiological heterogeneity. However, the divergent atypical neurodevelopment patterns in MDD remain poorly understood. Using a large multisite dataset and normative brain age prediction models, we identified two subgroups of patients with either accelerated or delayed brain development, each of which exhibited distinct functional topography—in particular, divergent expansion of the salience network (SAL). These patterns were associated with different clinical profiles and gene expression signatures. Notably, brain age in the default mode network responded to antidepressant treatment in both groups. These findings reveal heterogeneous neurodevelopmental trajectories in MDD and inform future efforts toward identifying biomarkers for personalized treatment evaluation.

Major depressive disorder (MDD) is a pervasive psychiatric condition that affects individuals from adolescence through late adulthood, with global prevalence rates estimated at approximately 3.7% among adolescents and 5% among adults (1, 2). An increasing number of in vivo neuroimaging studies have revealed that MDD is associated with significant disruptions in functional brain networks across the lifespan (3, 4), suggesting that this disorder may interfere with the typical development of brain networks. However, the complex relationship between MDD and brain development across the lifespan remains largely unexplored.

Throughout the lifespan, the human brain network undergoes continuous reorganization, following heterogeneous, nonlinear developmental trajectories at both regional and global scales (5, 6). This dynamic process supports the emergence and refinement of cognitive functions and emotional regulation (7, 8). Recently, the concept of "brain age" has emerged as a quantitative marker of brain maturation derived from structural or functional neuroimaging data (9, 10). In practice, machine learning models are trained to predict chronological age from brain features in a normative cohort and then applied to new individuals to estimate their brain age (9). The difference between predicted and chronological age, referred to as the brain age gap (BAG), captures whether an individual's brain appears to be developmentally advanced or delayed relative to normative trajectories (9). Growing evidence suggests that the BAG reflects microscale biological mechanisms, including genetic architecture (11) and plasma proteomics (12), and is associated with cognitive performance (13), positioning it as an integrative marker of brain health. Elevated BAG, indicating accelerated brain development or aging, has been reported across multiple

[1]A complete list of the DIDA-MDD Working Group can be found in the *SI Appendix*.

[2]To whom correspondence may be addressed. Email: mxia@bnu.edu.cn.

This article contains supporting information online at https://www.pnas.org/lookup/suppl/doi:10.1073/pnas.2519586123/-/DCSupplemental.

Published March 11, 2026.

psychiatric conditions (10, 14). In MDD, group-level BAG increases of approximately 1 to 4 y have been observed (15–18), with age-dependent variability in effect size, particularly between midlife and older adulthood (19). These findings highlight the need to examine the BAG within a lifespan neurodevelopmental framework.

While these studies have laid a foundation for understanding atypical brain development in MDD, several important limitations remain. First, traditional brain age models typically relied on group-level atlases to extract features (e.g., functional connectivity), thereby neglecting interindividual variability in the spatial distribution of functional networks (20, 21). More recent approaches using individualized functional indices have shown improved predictive performance (22). Additionally, recent precision functional mapping studies have revealed stable yet heterogeneous patterns of SAL expansion across individuals with MDD, indicating that SAL topographic deviations manifest in distinct individualized configurations (23). Such variability may be obscured by group-level parcellations. Accordingly, individualized functional topography enables more accurate characterization of person-specific network organization, allowing brain age prediction models to more sensitively detect atypical neurodevelopmental trajectories in patients with MDD. Second, MDD is characterized by substantial neurobiological and clinical heterogeneity (24). Recent studies have identified distinct neurophysiological subtypes in MDD (3, 25), yet prior group-level brain age analyses have largely overlooked the bidirectionality of the BAG. Both positive and negative BAGs, indicating accelerated and delayed brain aging, respectively, have been associated with different lifestyle factors (13) and even divergent survival curves in the general population (26), suggesting that these opposing deviations may have distinct biological and clinical implications. Therefore, mapping these divergent neurodevelopmental trajectories in MDD may offer critical insights into illness progression and help identify critical therapeutic windows. Finally, although genome-wide association studies (GWAS) have demonstrated that BAG is a heritable trait linked to several genetic loci (11, 14), the transcriptional mechanisms underlying BAG-related brain alterations, particularly in MDD, remain poorly understood. Elucidating the gene expression profiles associated with heterogeneous neurodevelopmental patterns in MDD could yield crucial insights into the molecular pathways underlying atypical brain maturation in this disorder.

To address these pivotal issues, we developed a brain age prediction model using a large, multisite resting-state fMRI (rs-fMRI) dataset comprising 2,170 participants, with individualized functional topography serving as input features. Patients with MDD were stratified into two subgroups on the basis of the directionality of their BAG. We then examined the functional network abnormalities, development trajectories, clinical characteristics, gene expression profiles, and treatment responses within each subgroup, thereby demonstrating the presence of heterogeneous neurodevelopmental patterns in MDD. Finally, we confirmed the robustness of our findings through multiple validation strategies.

Results

Datasets. This study utilized three independent rs-fMRI datasets. Dataset 1 included data from 1,065 healthy controls (HCs) and 1,105 patients with MDD (age range: 11 to 64 y, *SI Appendix*, Table S1), collected across nine research centers through the DIDA-MDD working group (27). This dataset served as the main exploration dataset for developing a normative brain age prediction model (Fig. 1*A*) and examining the heterogeneity of brain age deviations in MDD patients (Fig. 1 *B* and *C*). For individualized feature generation, we used Dataset 2 which consisted of rs-fMRI data from 146 healthy young individuals (*SI Appendix*, Table S2) to generate a group-level voxel-wise functional network parcellation reference (28). Finally, an additional analysis was conducted on Dataset 3, which consisted of 43 MDD patients who received six months of paroxetine treatment (*SI Appendix*, Table S3) to explore the relationship between brain age heterogeneity and treatment outcomes (Fig. 1*C*). The collections for all the datasets were approved by the ethics committees of their respective research centers, and written informed consent was obtained from all the participants (see the *SI Appendix* for details). All the rs-fMRI data were acquired using 3.0-T MRI scanners (*SI Appendix*, Table S4) and preprocessed following a standardized pipeline with strict quality control (29).

The BAG in Patients With MDD. To precisely characterize individualized functional networks and construct robust brain age prediction models, we first delineated participant-specific voxel-wise functional networks in volumetric (MNI152) space using a sparsity-regularized nonnegative matrix factorization (NMF) method (30). This approach yielded probabilistic parcellations for the 17 canonical cortical networks and one subcortical network, referred to as individualized functional topography maps. Each map reflects the spatial extent of the corresponding functional networks (see *Materials and Methods* for details and the *SI Appendix*, Fig. S1). Using whole-brain topography maps derived from HCs as features, we established a brain age prediction model based on support vector regression (SVR) and achieved high accuracy in predicting chronological age through a 20-fold cross-validation procedure [see *Materials and Methods* for details, adjusted mean absolute error (MAE) = 4.69, R = 0.78, $P < 0.001$; Fig. 2*A*]. At each site, the adjusted MAEs ranged from 4.14 to 5.63 (*SI Appendix*, Table S5), with no significant differences across sites (F = 0.94, $P = 0.49$; *SI Appendix*, Fig. S2), indicating the high robustness of this model. Additionally, we constructed brain age models based on the topography map of each functional network. Despite the significant predictors (all Ps < 0.001), the performance of the single-network models was inferior to that of the whole-brain model (*SI Appendix*, Fig. S3). Thus, we applied the whole-brain model to estimate brain age in MDD patients and calculated the BAG as the difference between the predicted age and chronological age. The whole-brain topography model revealed a significantly larger BAG in MDD patients than in HCs (T = 4.76, Cohen's $d = 0.14$, $P < 0.001$; Fig. 2*B*), indicating an overall "older" brain in MDD patients.

The BAG Reveals Distinct Growth Trajectories of Functional Topography Across the Lifespan in MDD. Although MDD patients exhibited an overall older brain, considerable heterogeneity in the BAG was also observed. Among the patients, 632 (57%) displayed a positive BAG (BAG+), indicating an older brain, while 473 (43%) had a negative BAG (BAG–), suggesting a younger brain. The results from single-topography brain age prediction models were largely consistent with those from whole-brain models: BAG+ patients exhibited significantly larger BAGs than HCs did in 16 single-network models, whereas BAG– patients demonstrated significantly smaller BAGs in 13 models (FDR-corrected q < 0.05; Fig. 2*C* and *SI Appendix*, Table S6). To further explore the functional network substrates related to the BAG, we divided all patients into BAG+ and BAG– groups and examined the correlations between topography loading and absolute BAG values. In BAG+ patients, positive correlations were primarily observed in the bilateral dorsolateral prefrontal cortex (dlPFC)

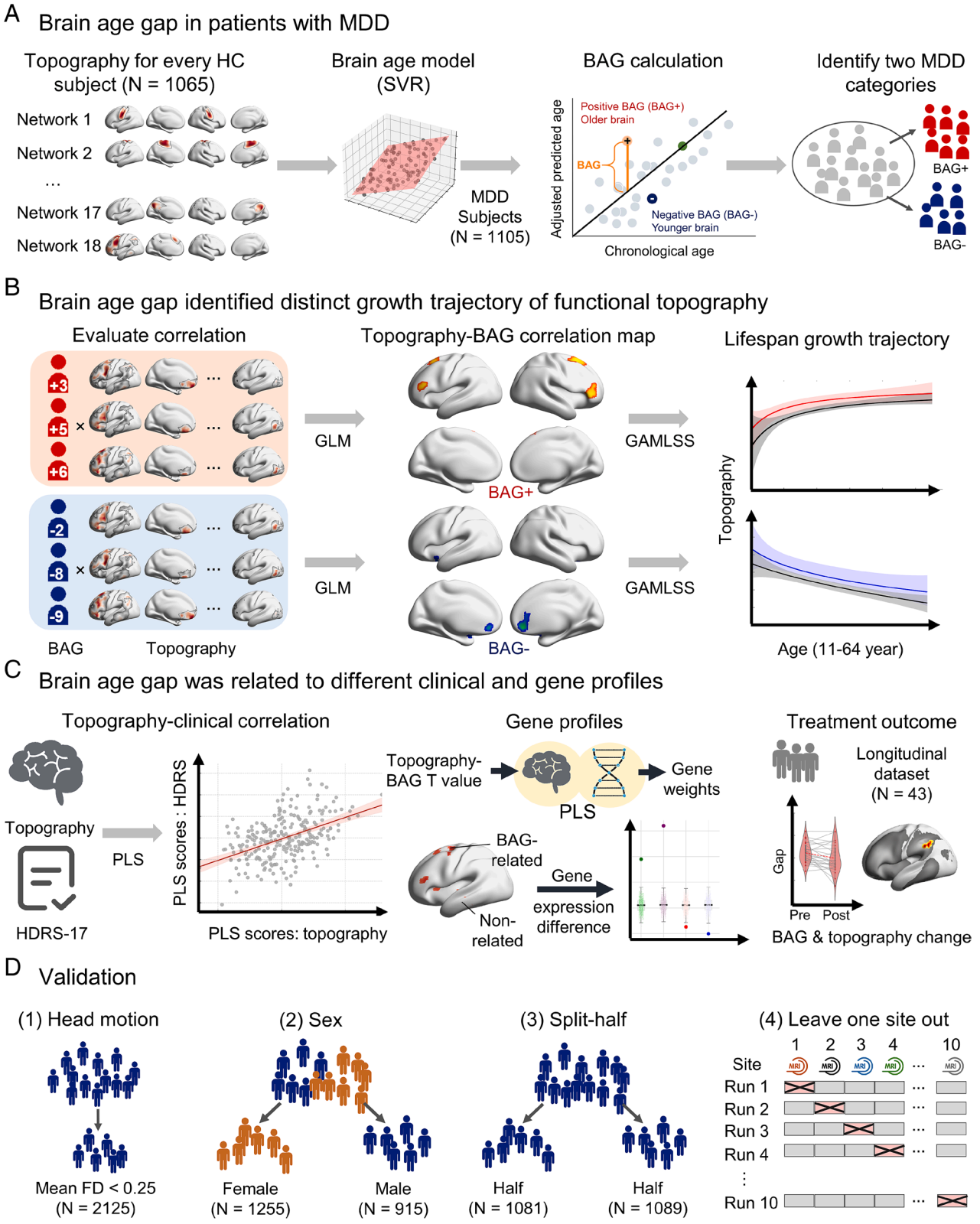

Fig. 1. Overview of the present study. (*A*) Classification of two MDD groups with oppositely signed BAGs. (*B*) Identification of distinct growth trajectories of functional trajectory using BAG. (*C*) Different clinical and genetic characteristics between the two groups. (*D*) Evaluation of the robustness of the results. BAG, brain age gap; FD, framewise displacement; GAMLSS, Generalized Additive Models for Location, Scale and Shape; GLM, General Linear Model; HDRS, Hamilton Depression Rating Scale; PLS, Partial Least Squares; SVR, Support Vector Regression.

and ventrolateral prefrontal cortex (vlPFC) for SAL loading, whereas negative correlations were found in typical regions of the sensorimotor network (SMN), dorsal attention network (DAN), and frontoparietal network (FPN), including the primary motor cortex and right angular gyrus (voxel-level $P < 0.001$, GRF-corrected $P < 0.05$; Fig. 2 *D* and *E* and *SI Appendix*, Fig. S4 and Table S7). These findings suggest that SAL expansion to the dlPFC and vlPFC, in addition to contraction in the SMN, DAN, and

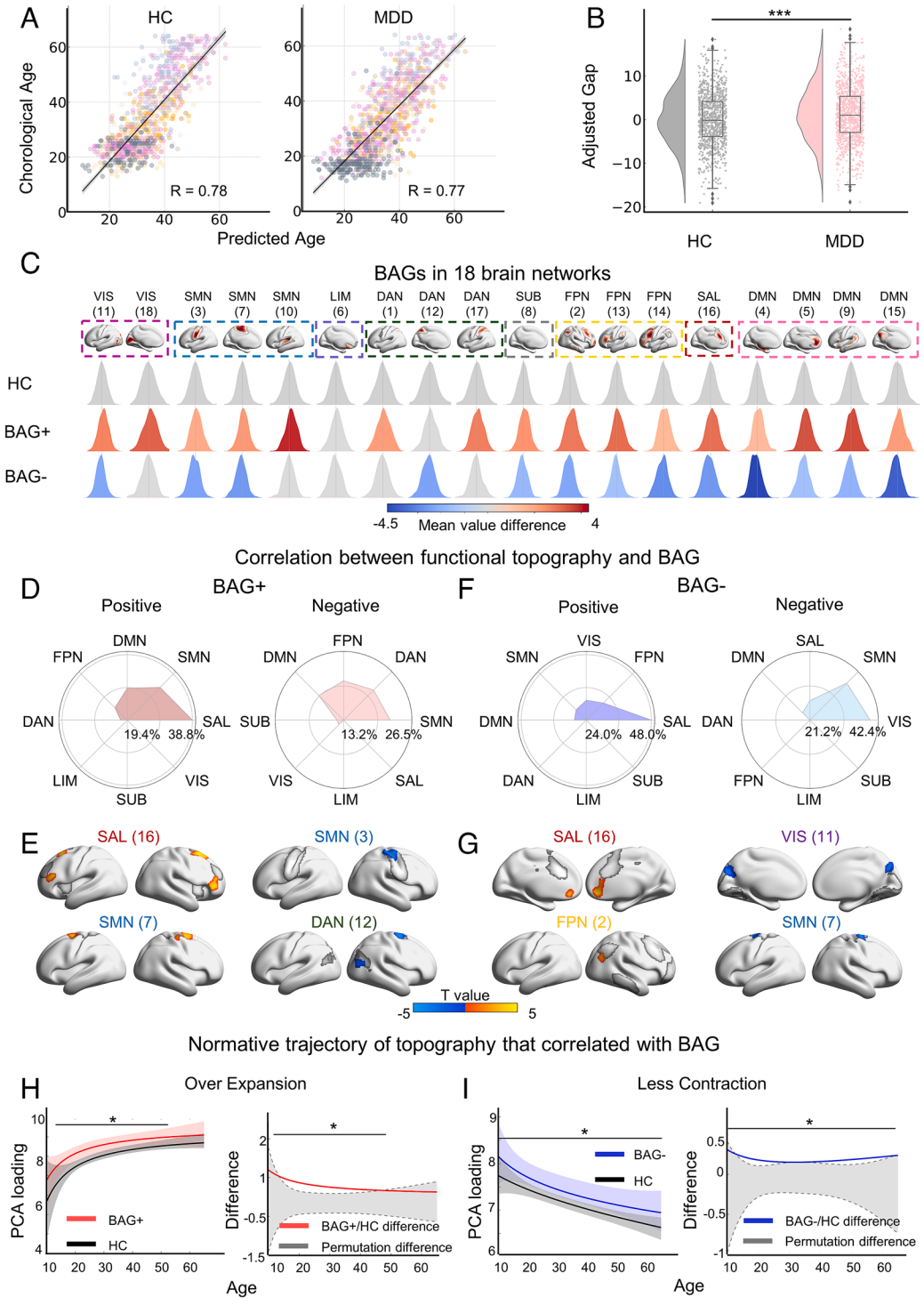

Fig. 2. Heterogeneous brain age in MDD patients. (*A*) Scatterplots show the correlation between chronological age and predicted brain age in the HC and MDD groups. Each circle represents an individual and its color indicates the scanning site. (*B*) The BAG in MDD was significantly higher than HCs (two-sample *t* test, $P < 0.001$). (*C*) Distribution of 18 brain network BAGs in HCs and two MDD categories. The colored distribution indicates that this BAG significantly differed from that of the HC group (one-way ANOVA, FDR-corrected $q < 0.05$, with post hoc multiple comparisons, $P < 0.05$). Darker colors reflect greater deviations. Network indices were derived from NMF; see *SI Appendix*, Fig. S1 for details. (*D*) BAG-related functional networks in BAG+ patients. The radar map represents the percentage in each system of total voxels with a significant correlation (voxel-level $P < 0.001$, GRF-corrected $P < 0.05$). To simplify the results, we combined the results from the 18 networks into 8 systems. (*E*) BAG-related regional functional topography in BAG+ patients. The correlation T value was mapped onto the brain surface, where colored voxels indicate those with a significant correlation to the BAG (voxel-level $P < 0.001$, GRF-corrected $P < 0.05$). Lighter colors indicate stronger correlations. For visualization purposes, only the most relevant networks are shown here; correlation maps for the remaining networks are provided in *SI Appendix*, Fig. S4. (*F*) BAG-related functional networks in BAG− patients. (*G*) BAG-related regional functional topography in BAG− patients. Correlation maps for the remaining networks are provided in *SI Appendix*, Fig. S5. (*H* and *I*). Distinct developmental trajectories of topography in the two groups. The *Left* panel shows lifespan trajectories of topography within BAG-related regions (voxel-level $P < 0.001$, GRF-corrected $P < 0.05$). Shaded areas indicate 95% CI estimated via 1,000 bootstrap resamples. The *Right* panel displays the average difference within each one-year interval of the fitting values between patients and HCs. Shaded areas represent the 95% interval derived from permutation tests. In both panels, the horizontal lines above the x-axis indicate age intervals with significant differences based on permutation testing. adj MAE, mean absolute error corrected by age; $*P < 0.05$; $***P < 0.001$; DAN, dorsal attention network; DMN, default-mode network; FPN, frontoparietal network; HC, healthy control; LIM, limbic network; MDD, major depressive disorder; n, sample size; R, Pearson correlation coefficient; SMN, sensorimotor network; SUB, subcortical; SAL, salience network; VIS, visual network.

FPN regions, contributes to a higher BAG in MDD. In contrast, BAG− patients showed positive correlations in the SAL loading within the bilateral medial orbitofrontal cortex (OFC), whereas negative correlations emerged in typical visual (VIS) and SMN areas, such as the medial occipital cortex and supplementary motor area (voxel-level $P < 0.001$, GRF-corrected $P < 0.05$; Fig. 2 *F* and *G* and *SI Appendix*, Fig. S5 and Table S8). These results indicate that SAL expansion into the OFC, along with contraction in the VIS and SMN, is associated with a lower BAG.

To characterize the lifespan developmental trajectories of topography for BAG-related regions, we applied principal component analysis (PCA) to extract the dominant topographic component in each group and used a generalized additive model for location, scale, and shape (GAMLSS) (31) to model their growth trajectories, with HCs as a reference. In BAG+ patients, the principal component of positively correlated topography rapidly increased from childhood to midlife, followed by a steady increase until older adulthood. Although this trajectory paralleled that of the HCs, it remained significantly higher between ages 13 and 50 ($P_{perm} < 0.05$, FDR corrected; Fig. 2*H*), indicating overexpansion and an accelerated neurodevelopmental trajectory. In BAG− patients, the principal component of positively correlated regions exhibited a nonlinear decrease from childhood to older adulthood. While this trajectory was similar in shape to that of HCs, BAG− patients consistently maintained significantly higher values across all ages ($P_{perm} < 0.05$, FDR corrected; Fig. 2*I*), reflecting reduced contraction and a delayed neurodevelopmental trajectory. Notably, no significant differences were observed in the trajectories of negatively correlated regions in either group. Overall, these results indicate that opposite BAGs in MDD patients are associated with distinct patterns of functional networks, which exhibit unique lifespan growth trajectories.

The BAG in MDD Is Related to Different Clinical Profiles. We also explored the clinical characteristics of BAG+ and BAG− MDD patients. First, we compared demographic and clinical variables, such as age, sex, illness duration, onset age, and overall HDRS scores (including its 17-item breakdown), between BAG+ and BAG− patients. The results indicated that BAG+ patients were significantly older and had longer illness durations than those of BAG− patients (Ps < 0.05; *SI Appendix*, Fig. S6). No significant differences were observed in the other variables. To assess the relationship between functional topography and clinical symptoms more comprehensively, we performed a partial least squares (PLS) correlation analysis between the topography maps and the 17-item HDRS scores within each MDD group. To address potential overfitting issues and improve generalizability, we applied a 10-fold cross-validation PLS method and evaluated the correlations across all the testing datasets. The significance of the PLS model was validated using permutation tests (1,000 times), whereas stable features were identified through the construction of 1,000 bootstrap resampled PLS models (see *Materials and Methods* for details). In BAG+ patients, functional topography was significantly correlated with HDRS-17 scores in the first PLS component (PLS1) ($R = 0.47$, $P_{perm} < 0.001$; Fig. 3*A*). The items related to mood, such as depressed mood and work and activities, exhibited the highest correlation weights (Fig. 3*B* and *SI Appendix*, Table S9). Stable brain regions primarily included the supramarginal gyrus, dlPFC, middle cingulate cortex, and inferior and middle temporal cortex, which are predominantly associated with the FPN, DMN, and DAN (Fig. 3*B*). In BAG− patients, topography was also significantly correlated with HDRS-17 scores in PLS1 ($R = 0.27$, $P_{perm} < 0.001$; Fig. 3*C*). The most prominent HDRS items were linked to insomnia problems, including middle and late insomnia (Fig. 3*D* and *SI Appendix*, Table S9).

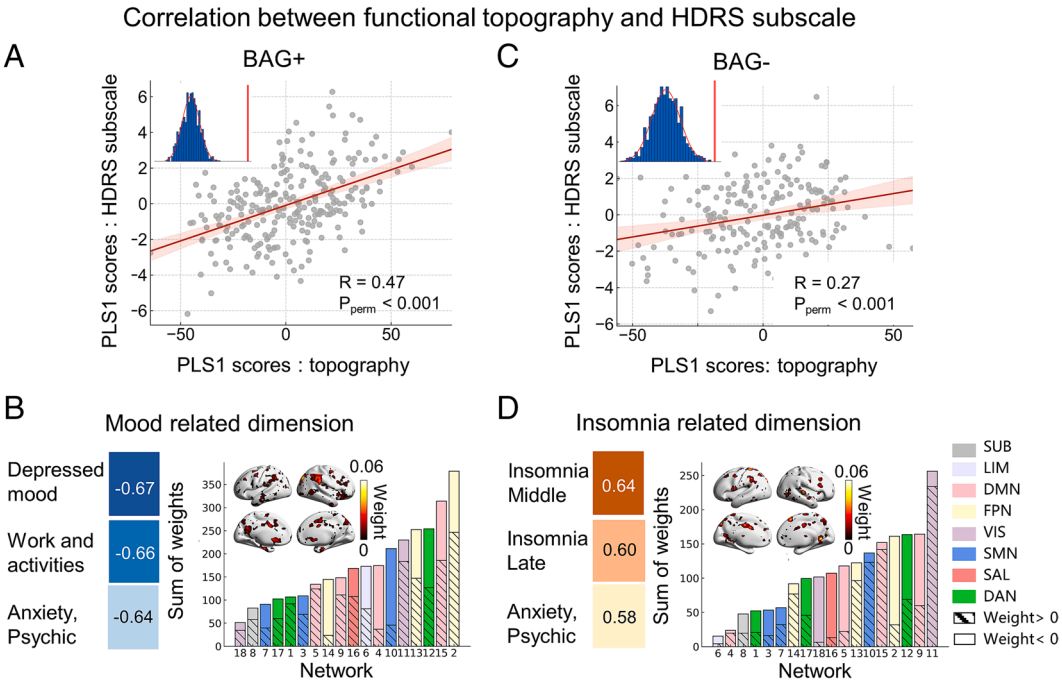

Fig. 3. Associations between topography and clinical profiles. (*A*) Scatterplots depict the correlation between functional topography scores and HDRS-17 scores for the first PLS dimension in BAG+ patients. The shadow indicates the 95% CI. Each dot represents a person. (*B*) PLS weights of features in BAG+ patients. The heatmaps (*Left*) show the top three items with the highest weights in PLS. The bar plots (*Bottom Right*) display the sum of voxel weights within each network that show a stable weight (bootstrapping 1,000 times, with the 95% CI not crossing zero), with solid bars representing weights <0 and hashed bars representing weights >0. The absolute value of the average stable weight across all networks was mapped onto the brain surface (*Top Right*). (*C*) Scatterplots depict the correlation between functional topography scores and HDRS-17 scores for the first PLS dimension in BAG− patients. (*D*) The PLS weights of features in BAG− patients. DAN, dorsal attention network; DMN, default-mode network; FPN, frontoparietal network; LIM, limbic network; SMN, sensorimotor network; SUB, subcortical; SAL, salience network; VIS, visual network.

Stable brain features were located mainly in the medial occipital, somatosensory, and auditory cortices, which are part of the VIS and DMN (Fig. 3*D*). These findings suggest that the two MDD categories exhibit distinct symptom-related neural mechanisms: emotional symptoms in BAG+ individuals are closely tied to high-order association networks, whereas sleep disturbances in BAG– individuals involve primary SMN.

The BAG in MDD Is Associated With Distinct Gene Expression Profiles. Next, we investigated the gene expression profiles associated with each MDD group to elucidate the potential molecular mechanisms underlying BAG heterogeneity. We analyzed the gene relevance of BAG-related brain maps using AHBA data (32) and examined their developmental characteristics using the BrainSpan Atlas (33). On the basis of genome expression data from six postmortem human brains in the AHBA datasets, we assessed the associations between the average topography-BAG correlation T-maps across 18 networks and transcriptional profiles using PLS. In BAG+ patients, PLS1 explained 21.4% of the variance in BAG–topography correlations ($P_{perm} < 0.001$, spatial autocorrelation corrected; Fig. 4*A*). The PLS1 score map represented a transcriptional profile with high expression mainly in prefrontal areas but low expression in primary areas, showing a spatial correlation with the BAG-related brain pattern (R = 0.46, $P_{perm} < 0.001$, spatial autocorrelation corrected; Fig. 4 *A* and *B*). We then ranked the normalized PLS1 weights and identified 558 PLS+ (Z > 3) and 1,202 PLS- (Z < –3) significant genes. Gene Ontology (GO) enrichment analysis revealed that PLS+ genes were enriched in terms such as "transporter complex," "dendritic tree," "mitochondrial membrane" and "synaptic signaling" (FDR-corrected q < 0.05; Fig. 4*B* and *SI Appendix*, Table S10), whereas PLS- genes were enriched in terms such as "centrosome," "kinase binding" and 'DNA damage response' (FDR-corrected q < 0.05; *SI Appendix*, Fig. S7 and Table S10). In BAG– patients, PLS1 accounted for 15.5% of the variance in the BAG–topography correlations (P_{perm} = 0.01, spatial autocorrelation corrected; Fig. 4*C*). The PLS1 score map represented a transcriptional profile characterized by high expression mainly in insula areas

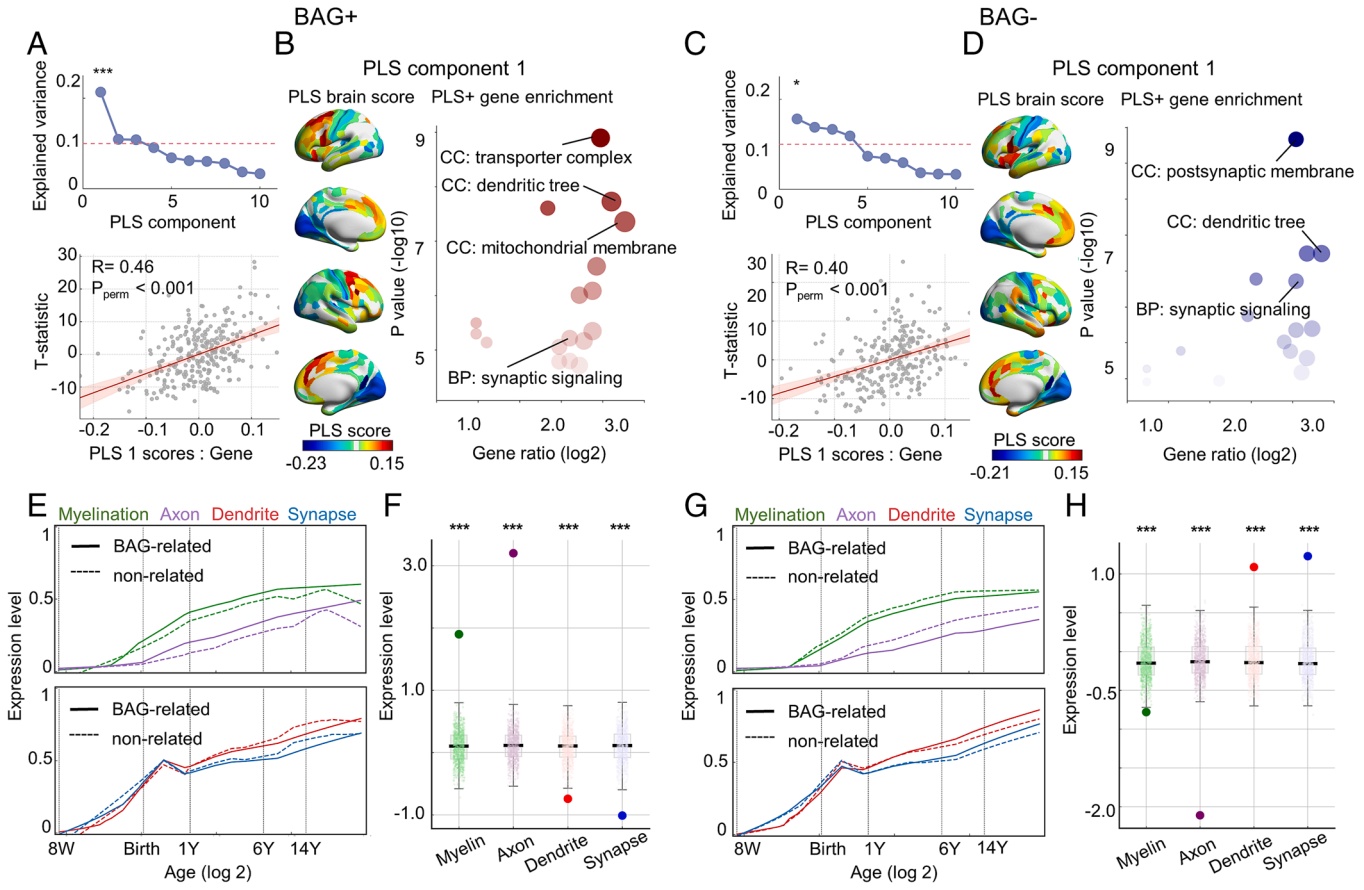

Fig. 4. Gene expression profiles of the two groups. (*A*) Association between the BAG-related brain map and gene expression in the BAG+ group. The *Top* panel shows the explained variance for the first 10 components obtained from the PLS analysis. The significant PLS component is marked with an asterisk. Scatterplots (*Bottom*) depict the correlation between the transcriptional profiles and the brain map for the first PLS component (PLS 1) in the BAG+ group. The shadow indicates the 95% CI. Each dot represents a brain region. (*B*) PLS 1 identified a gene expression profile with high expression mainly in the prefrontal areas but low expression in the primary areas (*Left*). The volcano plot (*Right*) depicts the Gene Ontology results for the biological processes, molecular functions, and cellular components of the PLS+ genes. The dots represent the GO terms corrected for multiple comparisons (FDR-corrected q < 0.05). The size of the dot indicates the number of genes belonging to the corresponding GO term, and the transparency of the dot represents the significance of the corresponding GO term. (*C*) Association between BAG-related brain map and gene expression in the BAG− group. (*D*) PLS 1 identified a gene expression profile with high expression mainly in the insula areas but low expression in the primary areas (*Left*). Volcano plot (*Right*) depicts GO results in PLS+ genes. (*E*) Transcriptomic trajectories between BAG-related regions (solid line) and other regions (dashed line) in four maturation processes in the BAG+ group. (*F*) Transcriptomic differences between BAG-related regions and other regions from childhood to adulthood in the BAG+ group. Boxes represent the interquartile range, with the median shown as a line inside the box, while the lower and upper boundaries of the box correspond to the 25th and 75th percentiles, respectively. The circles represent the actual differences. Scatter points represent the differences obtained through permutation testing. (*G*) Transcriptomic trajectories between BAG-related regions (solid line) and other regions (dashed line) in four maturation processes in the BAG− group. (*H*) Transcriptomic differences between BAG-related regions and other regions from childhood to adult in the BAG− group. **P* < 0.05, ****P* < 0.001; BP: Biological Process; CC: Cellular Component; MF: Molecular Function.

but low expression in primary areas, spatially correlating with the BAG-related brain pattern (R = 0.40, P_{perm} < 0.001, spatial autocorrelation corrected; Fig. 4 *C* and *D*). GO enrichment analysis revealed that 360 PLS+ (Z > 3) genes were enriched in terms such as "postsynaptic membrane," "dendritic tree," and "synaptic signaling" (FDR-corrected q < 0.05; Fig. 4*D* and *SI Appendix*, Table S11), whereas 1,418 PLS- (Z < −3) genes were enriched in terms such as "ensheathment of neurons," "kinase binding," and "myelin sheath" (FDR-corrected q < 0.05; *SI Appendix*, Fig. S7 and Table S11). Most terms remained significant in separate analyses of the left hemisphere (*SI Appendix*, Fig. S8).

To explore genetic associations during development, we utilized the BrainSpan Atlas (33), which includes gene expression samples from brain tissues ranging from 8 postconception weeks to 40 y of age. We first selected four gene sets representing key aspects of brain maturation (34). The brain tissue samples were divided into BAG-related regions and non-BAG-related regions based on the BAG-correlation map (*SI Appendix*, Fig. S4 and S5). After calculating the first principal component score of each gene set's transcription level, we fitted the transcriptomic trajectories and calculated the difference between BAG-related and non-BAG-related regions (see *Materials and Methods* for details). In the BAG+ group, distinct transcriptomic trajectories were observed in myelination and axon development after birth and in dendrite and synapse development from middle childhood to adolescence (Fig. 4*E*). BAG-related regions presented increased expression for myelination and axon development but decreased expression for dendrite and synapse development (P_{perm} < 0.001; Fig. 4*F*). In the BAG− group, divergent transcriptomic trajectories were evident in myelination and axon development from childhood to adolescence and in dendrite and synapse development from middle childhood to adulthood (Fig. 4*G*). BAG-related regions presented lower expression of myelination and axon development but greater expression of dendrite and synapse development (P_{perm} < 0.001; Fig. 4*H*). These findings indicate that oppositely signed BAGs are associated with distinct gene expression mechanisms and spatiotemporally specific transcriptional patterns of neurodevelopment.

The BAG and Distinct Treatment Outcomes in MDD. To investigate the impact of oppositely signed BAGs on treatment outcomes, we analyzed a dataset comprising 43 MDD patients with documented follow-up treatment results (BAG+: n = 25, BAG−: n = 18). Initially, we assessed categorical differences in longitudinal BAG changes using two-way repeated measures ANOVA. A significant category-by-treatment interaction emerged within the posterior DMN BAG (F = 16.20, FDR-corrected q < 0.05; Fig. 5*A*). Post hoc analyses revealed that the BAG of the posterior DMN significantly decreased after treatment in BAG+ patients (*P* = 0.003), whereas it significantly increased in BAG− patients (P = 0.013), indicating a normalizing effect of medical treatment on BAGs. Additionally, in BAG+ patients, an increase in the bilateral FPN BAG was positively correlated with improvements in the HDRS (R = 0.70, *P* < 0.001; Fig. 5*B*). Furthermore, the functional topography in the supramarginal gyrus (part of the FPN) and inferior temporal cortex (within the auditory SMN) significantly decreased after treatment in the BAG+ group (voxel-level *P* < 0.001, GRF-corrected *P* < 0.05; Fig. 5*C*). These findings suggest that both the FPN topography and its BAG are sensitive to pharmacological intervention.

Sensitivity Analyses. To validate the heterogeneous lifespan development observed in MDD patients, we conducted a sensitivity analysis using four strategies (see *SI Appendix* for details): i) To control for the influence of head motion, we repeated the main analysis with a stricter motion threshold [mean framewise displacement (FD) < 0.25 mm]. ii) To account for sex differences, we performed separate analyses for males and females. iii) To assess the reproducibility of our findings, we employed a split-half replication strategy. iv) To examine the potential influence of specific sites, we conducted leave-one-site-out analyses. We statistically compared the validation results and the main results by assessing the consistency of BAG differences between MDD patients and HCs, evaluating the overlap in subject classification, examining the spatial correlation of BAG-related brain maps, and examining the similarity of lifespan trajectories.

Specifically, we built the brain age prediction model for each validation strategy, confirming that functional topography significantly predicted chronological age across all the strategies (R = 0.74 ± 0.05; *SI Appendix*, Figs. S9–S14). Next, we performed a sensitivity analysis of the BAG for each participant. Consistently, the BAGs in the MDD patients remained significantly greater than those in the HCs across all the validation results (*SI Appendix*, Figs. S9–S13, and S15 and Table S12). We also reassigned the participants into two categories based on their BAG, with an average overlap rate of 90% between the validated and main classification indices (*SI Appendix*, Table S13). Furthermore, we assessed the association between the BAG and functional network topography. The correlation maps strongly aligned with the main findings (R = 0.83 ± 0.12 and R = 0.78 ± 0.13 for BAG+ and BAG− patients, P_{perm} < 0.001, spatial autocorrelation corrected; *SI Appendix*, Fig. S9–S13, and S16). Finally, we characterized the growth trajectories of the BAG-related topography, and the

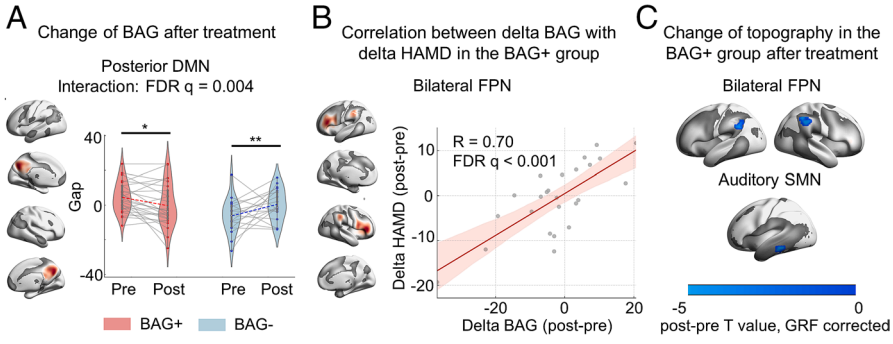

Fig. 5. Different treatment responses in the two groups. (*A*) Treatment effect on the BAG of the posterior DMN in the two groups after treatment. **P* < 0.05, ***P* < 0.01. (*B*) Scatterplots depict the correlation between the delta BAG of the bilateral FPN and the delta HDRS in the BAG+ group. The shadow indicates the 95% CI. Each dot represents a person. (*C*) Effects of treatment on the functional topography of the bilateral FPN and auditory SMN in the BAG+ group. The T value was mapped onto the brain surface, where colored voxels indicate those with significant changes (paired *t* test, voxel-level *P* < 0.001, GRF-corrected *P* < 0.05). A lighter color represents a greater change. DMN, default-mode network; FPN, frontoparietal network; SMN, sensorimotor network.

validated trajectories were highly similar to the main trajectories (R = 0.98 ± 0.05 and R = 0.98 ± 0.02 for BAG+ and BAG– patients, $P < 0.001$; *SI Appendix*, Fig. S9–S13, and S17 and Table S14).

To confirm the disease specificity of our findings, we examined whether the BAG–topography association observed in MDD could be attributed to normal development variance. No overlap was found between the BAG-related topography in HCs and that in MDD patients (*SI Appendix*, Fig. S18), suggesting that the observed BAG-related regions are specific to MDD.

Discussion

Using individualized functional features within a brain age prediction framework, we examined how MDD interacts with normative brain development over the lifespan. While prior brain age studies based on structural measures have reported an overall accelerated brain aging pattern in MDD, the substantial interindividual variability of the BAG was highly overlooked (15, 16, 18). Our work fills this gap by stratifying patients according to BAG direction and revealing two distinct patterns of deviation from typical neurodevelopment, each characterized by unique topography–BAG associations, neurodevelopment trajectories, clinical profiles, gene expression signatures, and treatment responses. These findings demonstrate that the BAG provides more than a summary index of neurodevelopmental deviation in MDD, and offers a mechanistic framework for probing the network-level, clinical, and molecular correlates of atypical brain maturation.

Oppositely Signed BAGs in MDD Reflects Distinct Functional Network Substrates. In both groups, SAL expansion was associated with greater deviation from normative brain development, suggesting that the SAL may serve as a shared pathological core. These findings align with previous findings indicating that SAL expansion is a stable feature of depression (23). However, the expansion patterns differed between the two groups. In BAG+ patients, the borders of the SAL extended toward the dlPFC and vlPFC—regions within the FPN—indicating increased SAL–FPN integration, which was associated with increased brain age. These findings align with prior reports of increased SAL–FPN connectivity in MDD (35, 36). The attention network helps reorient attention to salient stimuli and regulate the dynamic balance between high-order systems (37). According to the triple-network model, overintegration between the SAL and FPN may reflect maladaptive allocation of attentional resources toward the FPN, resulting in abnormal cognitive control of the FPN (37). An animal study demonstrated that abnormal frontal cortex activity—part of the FPN—is associated with excessive synaptic pruning (38), a process associated with cognitive decline and accelerated brain aging (39). Our results provide evidence that accelerated brain aging in MDD is associated with aberrant cognitive control within the FPN. Conversely, BAG– patients showed SAL expansion toward the medial OFC, accompanied by lower brain age. This pattern suggests enhanced SAL-limbic integration, a phenomenon also reported in prior MDD connectivity studies (40). Structural imaging studies have also reported reduced gray matter volume and cortical thickness in the medial OFC in MDD (41, 42). These convergent findings suggest that altered SAL–limbic coupling may contribute to disrupted salience detection of reward-related signals, ultimately impacting OFC-centered reward circuitry in MDD (37). Notably, disruptions within reward-related networks have been consistently associated with delayed brain maturation across psychiatric disorders (43), underscoring their relevance to neurodevelopmental alterations. In the BAG+ group, contraction of higher-order networks such as the FPN, DAN, and DMN was linked to an older brain, which is consistent with weakened within-network integration of these networks in MDD (36, 44). In contrast, in the BAG– group, contraction of primary networks such as the VIS and SMN contributed to a younger-appearing brain, likely reflecting reduced within-network connectivity. This pattern is consistent with prior reports of altered functional connectivity in these networks (36, 45). Evidence from other imaging modalities further supports these abnormalities, including reduced amplitude of low-frequency fluctuations in the visual system (46), as well as altered white matter functional gradients involving lower-order networks (47).

Using the same datasets, our previous studies revealed multilevel abnormalities in MDD, ranging from local brain activity to large-scale functional network architecture (27, 29, 45, 48), with a primary focus on group-level functional alterations. More recently, by adopting a normative modeling framework, we shifted the focus from group averages to interindividual variability and identified two biologically meaningful neurophysiological subtypes of MDD characterized by opposing patterns of connectivity deviation (3). The present study further extends this line of work by developing a harmonized multicenter brain age prediction model based on personalized functional topography, enabling the characterization of heterogeneous brain development trajectories in MDD and offering insights from a lifespan neurodevelopmental perspective on MDD.

The BAG in MDD Reveals Heterogeneous Lifespan Trajectories. While previous studies focused on brain growth trajectories in healthy individuals (5, 6), our study delineates the developmental curves of functional networks in patients with MDD.

In BAG+ patients, BAG-related regions showed significant accelerated growth that persisted from ages 13 to 50. Previous brain age studies have also reported accelerated brain aging in patients with MDD based on mixed-age samples (15–18), with a focus on overall group differences between patients and HCs. Notably, previous research has shown that brain age deviations in MDD may vary across different stages of life (19). Therefore, our study provides age-stratified evidence of brain aging patterns in MDD. Furthermore, although late-life depression (LLD) is commonly accompanied by cognitive decline and dementia risk (49), we observed no significant acceleration in brain aging beyond age 50. These findings support the hypothesis that neurobiological changes precede cognitive decline (50) and highlight midlife as a key window for intervention.

Previous brain age studies in MDD often combined patients with positive and negative BAGs, thereby overlooking the distinct brain age deviations present in BAG– individuals. In BAG– patients, significantly delayed brain growth was observed across all ages. During typical adolescence, prefrontal gray matter volume decreases (5). Consequently, the increased prefrontal gray matter volume observed in MDD adolescents was interpreted as a sign of delayed neurodevelopment (51). Our study extended these findings based on the neurodevelopmental trajectory. In later life, LLD is often characterized by accelerated cognitive and physiological aging processes (52). The delayed brain development observed in this group may reflect a compensatory mechanism.

The BAG in MDD Is Related to Divergent Clinical Profiles. Interestingly, although symptom severity did not differ, topography–symptom associations differed between two groups. In the BAG+ group, mood symptoms were most strongly linked to the topography of the dlPFC and supramarginal gyrus. The dlPFC supports top–down regulation of negative affect

(53), and previous studies have shown that its dysfunction impairs individuals' ability to attenuate unpleasant experiences, contributing to mood disturbances (54). The right supramarginal gyrus has been implicated not only in emotion recognition (55) but also in abnormal empathic processing (56). Specifically, this region has been associated with emotional egocentricity bias—a tendency to inappropriately project one's own emotional state onto others (56)—which may contribute to a self-reinforcing cycle of negative affect that ultimately exacerbates mood symptoms in MDD patients.

In the BAG– group, insomnia was most strongly associated with the topography of the visual, somatosensory, and supplementary motor cortices. The hyperarousal model of insomnia posits that acute stressors and associated cognitive rumination heighten cognitive and physiological arousal, further improving sensory processing and ultimately disrupting the ability to initiate or maintain sleep (57). Neuroimaging studies have also reported sensory–motor hyperconnectivity in patients with insomnia (58), which is consistent with our findings. Thus, while symptoms may be similar, their neurobiological underpinnings may vary between the two groups, indicating that category-specific mechanisms influence clinical presentation.

Notably, we observed a dissociation between neurodevelopmental deviations (most pronounced in the SAL) and symptom-related associations (primarily involving the FPN, DMN, DAN, VIS, and SMN). SAL-centered developmental divergence likely reflects early neurodevelopmental vulnerability, potentially involving altered maturation of salience detection, attentional reorientation, and affective processing systems (37). In contrast, symptom-related network alterations may represent downstream functional consequences of this developmental divergence that emerge during active symptom expression. This distinction suggests that developmental and symptomatic components of MDD may rely on partially dissociable neural systems, highlighting the need for interventions that address not only symptoms but also atypical neurodevelopmental processes.

The BAG in MDD Is Linked to Distinct Molecular Signatures. Both groups were enriched in terms related to signal transmission, such as dendritic tree and synaptic signaling, suggesting a common gene expression basis. Notably, given their central role in receiving, integrating, and transmitting neuronal signals to support interneuronal communication, dendritic and synaptic pathologies are hallmark features of many neuropsychiatric disorders (59). Previous studies have shown that reduced dendritic density occurs in the CA3 region of the hippocampus in individuals with anxiety and depression (60). Decreased expression of synaptic signaling proteins has also been reported in MDD patients (61). In animal models, chronic stress leads to elevated glucocorticoid levels in the hippocampus, which induce dendritic atrophy and synapse density through the use of the excitatory neurotransmitter glutamate (62). Chronic stress also reduces the expression of brain-derived neurotrophic factor (BDNF), contributing to abnormalities in dendritic structure and synaptic density (61).

Moreover, the two groups also exhibited distinct gene expression profiles. In the BAG+ group, the enriched terms were predominantly associated with energy regulation and metabolism, such as the mitochondrial membrane and the DNA damage response (DDR). Mitochondrial membranes are essential for maintaining the mitochondrial membrane potential (MMP) and ATP production, and their dysfunction has been implicated in abnormal brain aging (63). Reactive oxygen species (ROS) are harmful byproducts of oxidative metabolism. Accelerated aging of the brain leads to excessive ROS (64). As mitochondrial membranes are among the primary targets of ROS, this oxidative stress induces membrane depolarization (65). The DDR is a fundamental biological process that safeguards genomic stability and contributes to healthy aging (66). When the DDR is impaired, DNA damage can accumulate not only in nuclear DNA but also in mitochondrial DNA, leading to mitochondrial dysfunction (67). This dysfunction, in turn, results in energy deficits, oxidative stress, and disrupted cellular signaling—hallmarks of neurodegenerative diseases (68). BAG– patients showed enrichment of the myelination sheath. Neuroimaging studies have identified white matter myelination as a reliable indicator of functional brain maturation (69). Notably, reduced myelin content has been observed in individuals with delayed neurodevelopment (70), suggesting that aberrant myelination may underlie delayed brain development in this group. This study links brain age deviation to transcriptomic signatures in MDD.

Limitations and Future Directions. Several limitations of the current study should be acknowledged. First, integrating multimodal neuroimaging data—such as structural MRI and task-based fMRI data—may improve prediction accuracy and provide a more comprehensive understanding of neurodevelopmental deviations in MDD. Second, future longitudinal studies in patients with MDD are needed to track and validate neurodevelopmental trajectories directly over time. Third, although the scan duration in our dataset is comparable to that of previous large-scale MDD consortia (71–73), studies of individualized network mapping suggest that longer acquisitions can further improve reliability (21). Future work incorporating extended or multisession scans will therefore be important for enhancing the stability of individualized topography. Fourth, since the gene expression data were derived from postmortem brain samples of six donors, future research incorporating individual-level transcriptomic data should focus on clarifying the molecular underpinnings of brain aging in MDD. Fifth, our treatment dataset included only paroxetine responders. Future studies should prioritize data collection on a broader range of treatment responses to explore the impact of the BAG on treatment efficacy. Finally, incorporating cognitive measures could clarify the interplay among development, aging, and cognition in MDD.

Materials and Methods

Briefly, we analyzed multisite resting-state fMRI data from individuals with MDD and healthy controls. Individualized functional network topography was derived using a sparsity-regularized nonnegative matrix factorization approach. Brain age was estimated using machine-learning models trained on healthy controls, and deviations from normative development were quantified across the lifespan. Age-related trajectories were modeled using generalized additive models for location, scale, and shape. Associations with clinical profiles were assessed using PLS correlation, and transcriptional correlates were explored by integrating neuroimaging maps with gene expression data from the Allen Human Brain Atlas and BrainSpan dataset. The codes and all derived brain imaging metrics used in the analysis for this manuscript are available on GitHub (https://github.com/ALICE1029/topography_MDD) (74). Detailed descriptions of the datasets and methods are provided in the *SI Appendix*.

Ethical Statement. The study was approved by the ethics committees of each research center, and written informed consent was obtained from each participant. Specifically, in Dataset 1, data collection was approved by the following institutional ethics committees: Ethics Committee of the First Affiliated Hospital of China Medical University (CMU site); Human Investigation Committees of the Zhumadian Psychiatry Hospital and the Second Xiangya Hospital, Central South University (CSU site); Ethics Committee of the First Affiliated Hospital of Guangzhou University of Chinese Medicine (GCMU site); Ethics Committee of the First Affiliated Hospital of Kunming Medical University (KMU site); Ethics

Committee of Peking University Sixth Hospital (PKU site); Ethics Committee of West China Hospital, Sichuan University (SCU site); Institutional Review Board (IRB) of the Faculty of Psychology, Southwest University (SWU site); Human Investigation and Ethics Committees of Yang Ming University (YMU site); and Ethics Committee of the First Affiliated Hospital of Zhengzhou University (ZZU site). In Dataset 2, data collection was approved by the IRB of the State Key Laboratory of Cognitive Neuroscience and Learning at Beijing Normal University. In Dataset 3, data collection was approved by the Human Investigation Committees of the Zhumadian Psychiatry Hospital and the Second Xiangya Hospital, Central South University of China.

Preprocessing. rs-fMRI data were preprocessed using SPM12 (www.fil.ion.ucl.ac.uk/spm/) and SeeCAT (https://www.nitrc.org/projects/seecat/). To ensure signal stability, the initial ten volumes were discarded. Preprocessing included slice-timing correction and head-motion correction. The motion-corrected images were normalized to MNI space using an echo planar imaging (EPI) template, resampled to 3-mm isotropic voxels, and smoothed with a 6-mm full-width at the half-maximum Gaussian kernel. Linear trends were removed, and nuisance covariates, including the Friston–24 motion parameters, white matter and cerebrospinal fluid signals, were regressed from each voxel's time series. Temporal bandpass filtering (0.01 to 00.08 Hz) was then applied. To reduce motion-related artifacts, we performed scrubbing: any frame with a framewise displacement >0.5 mm, together with its neighboring frames (two forward, one backward), was replaced using linear interpolation.

Calculating Individualized Functional Network Topography. To derive the individualized functional network topography, we used the NMF method (30), which factors data by positively weighting elements that covary and generates a highly specific and reproducible parts-based representation. This method has been utilized for decomposing fMRI data to create individualized functional brain network soft atlases (30, 75). In this study, NMF decomposition was performed in volumetric (MNI152) space at the voxel level, using a gray-matter mask to constrain the decomposition to gray matter voxels.

Individual-specific networks were derived in two steps. 1) Group reference network. To avoid bias driven by outliers, we first generated a group reference atlas consisting of 18 networks (17 cortical networks and 1 subcortical network) using data from healthy young adults (Dataset 2). A bootstrap strategy was used: in each iteration, 80% of the subjects were randomly sampled, and their time series were concatenated. NMF was then applied to factor this matrix into a loading matrix V (18 × 45892 representing network topography) and a time series matrix. This procedure was repeated 50 times, resulting in the production of 50 group atlases. These atlases were subsequently combined into a single reference atlas using spectral clustering. 2) Individual networks. Using the group atlas for initialization, NMF was applied to each participant's own fMRI time series to derive individualized networks. The group atlas served as the initialization for V, which was then iteratively refined together with each participant's time-series matrix through the alternating optimization procedure–updating spatial maps, temporal weights, and regularization parameters until convergence (30). This procedure yielded a participant-specific loading matrix V (18×45892 matrix, representing their individualized voxelwise topography). Finally, to harmonize the data across different sites, we applied ComBat harmonization (76) to protect the group, age, sex, and mean FD as covariates of functional topography.

To further evaluate the stability of our individualized parcellations, we defined two seed regions consistently assigned to the DMN and SAL across 20 individuals (one HC and one patient per site) and generated seed-based connectivity maps. These maps robustly recovered canonical network patterns (*SI Appendix*, Fig. S19), indicating that the individualized parcellations capture stable functional organization rather than noise-driven variability.

Establishing the Brain Age Prediction Model. We predicted an individual's chronological age using a 20-fold cross-validation SVR model with functional topography maps as input features at both the whole-brain and single-network levels, with sex included as a covariate. To predict the chronological age of MDD patients, we retrained the SVR model on full sample of healthy individuals and applied the parameters to MDD patients. The performance of the model was evaluated based on the following two metrics: the MAE with age regressed and the Pearson correlation coefficient between the predicted and chronological age. The parameters in SVR were set to their default values. See the *SI Appendix* for details.

Estimating the Individual BAG. The BAG for each individual was calculated by subtracting the actual chronological age from the predicted age. Because the BAG was calculated from but did not capture individuals' chronological age, it was regressed from all estimated BAGs, and the residuals of this regression were defined as adjusted BAGs (10, 16). Specifically, we fitted a regression model between chronological age and predicted age in the training set. The slope and intercept of this model were subsequently used to adjust the predicted age in the testing set. After this age-bias correction, the BAG was independent of chronological age (*SI Appendix*, Fig. S20).

We used a two-sample *t* test to compare the differences in the whole-brain BAG between all the MDD patients and HCs. MDD patients with a BAG > 0 were categorized as individuals whose brains were older than normative, whereas those with a BAG < 0 were identified as individuals whose brains were younger. To validate these results, we also conducted one-way ANOVA to examine differences in network BAGs, between individuals in these two MDD categories and HCs. Networks showing statistical significance at FDR $q < 0.05$ were analyzed using post hoc tests.

Assessing the Association between Functional Topography and BAG. To assess the relationships between functional networks and distinct BAGs, we utilized a general linear model (GLM) to examine the correlation between the functional topography of 18 networks and the absolute value of the BAG in two MDD categories, with age, sex, and mean FD as covariates. The significance threshold was set to $P < 0.001$ at the voxel level, followed by Gaussian random field (GRF) correction (77) at the cluster level with $P < 0.05$. See the *SI Appendix* for details.

Modeling Growth Trajectories of Functional Topography across Lifespan. To characterize age-related changes in BAG-related functional topography, we first extracted the first principal component of the BAG-related topographic features using PCA. Age-related nonlinear trajectories were then modeled using GAMLSS (31), which was implemented in the gamlss package (version 5.4-3) in R 4.2.0. We used the Box–Cox t distribution, to model the empirical distribution of the data (78). The model estimates four parameters: location/median (μ), coefficient of variation (σ), skewness (ν), and kurtosis (τ). Following prior work (79), ν and τ were fitted as constants. The location parameter accounted for head-motion effects. Each phenotype *y* was modeled as follows:

$$y = BCT(\mu, \sigma, \nu, \tau),$$

$$\mu = f_{\mu}^{1}(age \times female) + f_{\mu}^{2}(age \times male),$$

$$\sigma = f_{\sigma}(age),$$

$$\nu = \beta_{\nu}, \tau = \beta_{\tau}.$$

To assess the robustness of the lifespan trajectory models, we performed bootstrap resampling with stratification by age and sex. Trajectory differences between each MDD group and HCs were quantified across one-year age intervals and evaluated using stratified permutation testing. See the *SI Appendix* for details.

Assessing the Associations Between Functional Topography and Clinical Symptoms. The relationships between topography and HDRS-17 item scores were evaluated using PLS correlation, which was validated through a 10F-CV procedure with age, sex, and mean FD regressed. To assess whether the correlation was significantly greater than expected by chance, 1,000 permutation tests were performed. To identify features stably contributing to PLS, we employed a bootstrapping strategy, constructing 1,000 PLS models using resampled datasets. We recalculated the PLS weights to obtain CIs for every feature. Stable features were defined as those whose 95% CIs did not cross zero. Finally, the feature contributions were ranked based on PLS weights derived from all the samples. See the *SI Appendix* for details.

Examining the Associations between Gene Expression and BAG-Related Functional Topography. To explore the transcriptional profiles underlying BAG-related functional networks in the two MDD categories, we utilized whole-brain microarray-based gene expression data from AHBA (32) and applied PLS regression to assess associations between these transcriptional profiles and average BAG-related brain maps across 18 networks in the two groups. Statistical

significance was determined using permutation tests with spatial–autocorrelation correction (80). For each significant component, bootstrapping identified genes with $|Z| > 3$, which were submitted to Gene Ontology enrichment analysis via Metascape (81) (https://metascape.org) to infer biological processes, molecular functions, and cellular components. We also validated the hemisphere effects by this connectome–transcriptome association analysis.

To investigate the developmental characteristics of BAG-related regions, we examined differences in transcription level between BAG-related regions and non-BAG-related regions for genes previously linked to key neurodevelopmental processes. Specifically, we utilized the BrainSpan dataset (33) and selected four gene sets (34), which cover typical maturation, including axon development, myelination, dendrite development, and synapse development. Gene expression trajectories were derived from the BrainSpan dataset using PCA and locally weighted regression. The significance of regional differences was assessed through permutation testing.

Exploring the Interactive Effects between BAGs and Antidepressant Treatments. To investigate whether patients in the identified MDD categories responded differently to treatment, a dataset that recorded the outcomes of patients who received a 6-mo antidepressant treatment with paroxetine was used (*SI Appendix*, Table S2). Patients were stratified into BAG+ and BAG− categories based on baseline BAGs. We tested whether treatment-induced BAG changes differed between categories using repeated-measures analyses, with correction for multiple comparisons. Post hoc analyses were conducted when appropriate. Associations between changes in the BAG (whole-brain BAG and 18 network BAGs) and HDRS scores were also assessed. In addition, treatment-related alterations in functional topography were evaluated. All analyses were adjusted for the effects of age, sex, and mean FD. See the *SI Appendix* for details.

Visualization. For visualization purposes, volumetric maps were projected onto the fsaverage 32 k cortical surface using voxel-to-vertex mapping implemented in BrainNet Viewer. Briefly, for each surface vertex, its corresponding coordinate in volumetric space was identified, and the functional value was computed using trilinear interpolation from neighboring voxels. This interpolated value was then assigned to the vertex to produce a surface-based rendering.

Data, Materials, and Software Availability. The original raw data (e.g., MRI images) are not publicly available due to data sharing agreements and privacy regulations. All derived brain imaging metrics used in the analysis (e.g., brain age gap, topography scores) and the analysis code will be made available in a persistent public repository upon publication. Data have been deposited in GitHub (https://github.com/ALICE1029/topography_MDD) (74).

ACKNOWLEDGMENTS. We thank Drs. Ruiwang Huang and Gaolang Gong from the State Key Laboratory of Cognitive Neuroscience and Learning and the IDG/McGovern Institute for Brain Research at Beijing Normal University, China, for their efforts in collecting and sharing Dataset 2, the Connectivity-based Brain Imaging Research Database (C-BIRD). We thank Dr. Zaixu Cui from Chinese Institute for Brain Research, China, for his suggestions in data analysis. This work was supported by STI 2030-Major Projects (2022ZD0211500 and 2021ZD0200500), Beijing Natural Science Foundation (JQ23033) and National Natural Science Foundation of China (82021004, 82071998, 82402368, T24B2012, 824B2051 and 82572350).

Author affiliations: [a]State Key Laboratory of Cognitive Neuroscience and Learning, Beijing Normal University, Beijing 100875, China; [b]Beijing Key Laboratory of Brain Imaging and Connectomics, Beijing Normal University, Beijing 100875, China; [c]International Data Group/McGovern Institute for Brain Research, Beijing Normal University, Beijing 100875, China; [d]School of Systems Science, Beijing Normal University, Beijing 100875, China; [e]Department of Psychiatry and National Clinical Research Center for Mental Disorders, The Second Xiangya Hospital of Central South University, Changsha, Hunan 410013, China; [f]Mental Health Institute of Central South University, China National Technology Institute on Mental Disorders, Hunan Technology Institute of Psychiatry, Hunan Key Laboratory of Psychiatry and Mental Health, Hunan Medical Center for Mental Health, National Technology Institute on Mental Disorders, Hunan Technology Institute of Psychiatry, Changsha, Hunan 410083, China; [g]Affiliated WuTaiShan Hospital of Medical College of Yangzhou University, Yangzhou Mental Health Centre, Yangzhou, Jiangsu 225003, China; [h]Affiliated Wuhan Mental Health Center, Huazhong University of Science and Technology, Wuhan, Hubei 430012, China; [i]Department of Psychiatry, Lanzhou University Second Hospital, Lanzhou, Gansu 730030, China; [j]Mental Health Education and Counseling Center, Shanghai University of Medicine and Health Sciences, Shanghai 201318, China; [k]Key Laboratory of Cognition and Personality (Southwest University), Ministry of Education, Chongqing 400715, China; [l]Department of Psychology, Southwest University, Chongqing 400715, China; [m]Department of Magnetic Resonance Imaging, The First Affiliated Hospital of Zhengzhou University, Zhengzhou, Henan 450052, China; [n]Key Laboratory of Brain Functional Genomics (Ministry of Education), Affiliated Mental Health Center (East China Normal University), School of Psychology and Cognitive Science, East China Normal University, Shanghai 200062, China; [o]Department of Radiology, The First Affiliated Hospital of Guangzhou University of Chinese Medicine, Guangzhou, Guangdong 510405, China; [p]Peking University Sixth Hospital, Peking University Institute of Mental Health, National Health Commission Key Laboratory of Mental Health (Peking University), National Clinical Research Center for Mental Disorders (Peking University Sixth Hospital), Peking University, Beijing 100191, China; [q]Department of Radiology, Huaxi MR Research Center, Institute of Radiology and Medical Imaging, West China Hospital of Sichuan University, Chengdu, Sichuan 610041, China; [r]Psychoradiology Key Laboratory of Sichuan Province, West China Hospital of Sichuan University, Chengdu, Sichuan 610041, China; [s]Xiamen Key Lab of Psychoradiology and Neuromodulation, Department of Radiology, West China Xiamen Hospital of Sichuan University, Xiamen, Fujian 361022, China; [t]Affiliated Mental Health Center and Hangzhou Seventh People's Hospital, Zhejiang University School of Medicine, Hangzhou, Zhejiang 310013, China; [u]Department of Psychiatry, First Affiliated Hospital of Kunming Medical University, Kunming, Yunnan 650032, China; [v]Institute of Science and Technology for Brain-Inspired Intelligence, Fudan University, Shanghai 200433, China; [w]Institute of Neuroscience, National Yang Ming Chiao Tung University, Taipei 112304, China; [x]Department of Education and Research, Taipei City Hospital, Taipei 103212, China; [y]Department of Psychiatry, The First Affiliated Hospital of China Medical University, Shenyang, Liaoning 110001, China; [z]Chongqing Key Laboratory of Neurobiology, Chongqing 400016, China; [aa]Department of Neurology, The First Affiliated Hospital of Chongqing Medical University, Chongqing 400016, China; and [bb]Chinese Institute for Brain Research, Beijing 102206, China

Author contributions: C.P. and M.X. designed research; C.P., X.S., J.Z., X. Liang, L.S., Q.L., J.S., X. Lu, Q.D., L.Z., X.W., D.W., Y. Chen, B.L., C.-C.H., Y.Z., Y.W., T.C., Y. Cheng, X.X., Q.G., T.S., S.Q., C.-P.L., J.C., Y.T., F.W., J.Q., P.X., L.L., Y.H., D.W., and M.X. performed research; C.P. and M.X. analyzed data; X.S. and Y.H. reviewed and edited the paper; J.Z., X. Liang, and L.S. provided guidance on data analysis and result interpretation; Q.L., J.S., X. Lu, Q.D., L.Z., X.W., D.W., Y. Chen, B.L., C.-C.H., Y.Z., Y.W., T.C., Y. Cheng, X.X., Q.G., T.S., S.Q., C.-P.L., J.C., Y.T., F.W., J.Q., P.X., L.L., and D.W. collected the data for this study; and C.P. and M.X. wrote the paper.

The authors declare no competing interest.

This article is a PNAS Direct Submission.

1. Anonymous, *Global Health Data Exchange* (Institute of Health Metrics and Evaluation, 2021).
2. B. Lu, L. Lin, X. Su, Global burden of depression or depressive symptoms in children and adolescents: A systematic review and meta-analysis. *J. Affect. Disord.* **354**, 553–562 (2024).
3. X. Sun *et al.*, Mapping neurophysiological subtypes of major depressive disorder using normative models of the functional connectome. *Biol. Psychiatry* **94**, 936–947 (2023).
4. Q. Gong, Y. He, Depression, neuroimaging and connectomics: A selective overview. *Biol. Psychiatry* **77**, 223–235 (2015).
5. R. A. I. Bethlehem *et al.*, Brain charts for the human lifespan. *Nature* **604**, 525–533 (2022).
6. L. Sun *et al.*, Human lifespan changes in the brain's functional connectome. *Nat. Neurosci.* **28**, 891–901 (2025).
7. X.-N. Zuo *et al.*, Human connectomics across the life span. *Trends Cogn. Sci.* **21**, 32–45 (2017).
8. B. J. Casey, A. S. Heller, D. G. Gee, A. O. Cohen, Development of the emotional brain. *Neurosci. Lett.* **693**, 29–34 (2019).
9. J. H. Cole, K. Franke, Predicting age using neuroimaging: Innovative brain ageing biomarkers. *Trends Neurosci.* **40**, 681–690 (2017).
10. Y. E. Tian *et al.*, Heterogeneous aging across multiple organ systems and prediction of chronic disease and mortality. *Nat. Med.* **29**, 1221–1231 (2023).
11. J. Wen *et al.*, The genetic architecture of multimodal human brain age. *Nat. Commun.* **15**, 2604 (2024).
12. W. S. Liu *et al.*, Plasma proteomics identify biomarkers and undulating changes of brain aging. *Nat. Aging* **5**, 99–112 (2025).
13. L. Baecker, R. Garcia-Dias, S. Vieira, C. Scarpazza, A. Mechelli, Machine learning for brain age prediction: Introduction to methods and clinical applications. *EBioMedicine* **72**, 103600 (2021).
14. T. Kaufmann *et al.*, Common brain disorders are associated with heritable patterns of apparent aging of the brain. *Nat. Neurosci.* **22**, 1617–1623 (2019).
15. L. K. M. Han *et al.*, Brain aging in major depressive disorder: Results from the ENIGMA major depressive disorder working group. *Mol. Psychiatry* **26**, 5124–5139 (2021).
16. L. K. M. Han *et al.*, Contributing factors to advanced brain aging in depression and anxiety disorders. *Transl. Psychiatry* **11**, 402 (2021).
17. Y. Luo, W. Chen, J. Qiu, T. Jia, Accelerated functional brain aging in major depressive disorder: Evidence from a large scale fMRI analysis of Chinese participants. *Transl. Psychiatry* **12**, 397 (2022).
18. K. Dunlop, L. W. Victoria, J. Downar, F. M. Gunning, C. Liston, Accelerated brain aging predicts impulsivity and symptom severity in depression. *Neuropsychopharmacology* **46**, 911–919 (2021).
19. S. Christman *et al.*, Accelerated brain aging predicts impaired cognitive performance and greater disability in geriatric but not midlife adult depression. *Transl. Psychiatry* **10**, 317 (2020).
20. M. Li *et al.*, Performing group-level functional image analyses based on homologous functional regions mapped in individuals. *PLoS Biol.* **17**, e2007032 (2019).
21. E. M. Gordon *et al.*, Precision functional mapping of individual human brains. *Neuron* **95**, 791–807. e797 (2017).
22. Z. Zhou *et al.*, Multiscale functional connectivity patterns of the aging brain learned from harmonized rsfMRI data of the multi-cohort iSTAGING study. *Neuroimage* **269**, 119911 (2023).
23. C. J. Lynch *et al.*, Frontostriatal salience network expansion in individuals in depression. *Nature* **633**, 624–633 (2024).

24. C. J. Lynch, F. M. Gunning, C. Liston, Causes and consequences of diagnostic heterogeneity in depression: Paths to discovering novel biological depression subtypes. *Biol. Psychiatry* **88**, 83–94 (2020).
25. A. T. Drysdale *et al.*, Resting-state connectivity biomarkers define neurophysiological subtypes of depression. *Nat. Med.* **23**, 28–38 (2017).
26. J. H. Cole *et al.*, Brain age predicts mortality. *Mol. Psychiatry* **23**, 1385–1392 (2018).
27. M. Xia *et al.*, Connectome gradient dysfunction in major depression and its association with gene expression profiles and treatment outcomes. *Mol. Psychiatry* **27**, 1384–1393 (2022).
28. Q. Lin *et al.*, A connectivity-based test-retest dataset of multi-modal magnetic resonance imaging in young healthy adults. *Sci. Data* **2**, 150056 (2015).
29. M. Xia *et al.*, Reproducibility of functional brain alterations in major depressive disorder: Evidence from a multisite resting-state functional MRI study with 1, 434 individuals. *Neuroimage* **189**, 700–714 (2019).
30. H. Li, T. D. Satterthwaite, Y. Fan, Large-scale sparse functional networks from resting state fMRI. *Neuroimage* **156**, 1–13 (2017).
31. D. M. Stasinopoulos, R. A. Rigby, Generalized additive models for location scale and shape (GAMLSS) in R. *J. Stat. Softw.* **23**, 1–46 (2007).
32. M. J. Hawrylycz *et al.*, An anatomically comprehensive atlas of the adult human brain transcriptome. *Nature* **489**, 391–399 (2012).
33. J. A. Miller *et al.*, Transcriptional landscape of the prenatal human brain. *Nature* **508**, 199–206 (2014).
34. H. J. Kang *et al.*, Spatio-temporal transcriptome of the human brain. *Nature* **478**, 483–489 (2011).
35. T. Ye *et al.*, Altered functional connectivity of the dorsolateral prefrontal cortex in first-episode patients with major depressive disorder. *Eur. J. Radiol.* **81**, 4035–4040 (2012).
36. N. Y. Tse *et al.*, A mega-analysis of functional connectivity and network abnormalities in youth depression. *Nat. Mental Health* **2**, 1169–1182 (2024).
37. V. Menon, Large-scale brain networks and psychopathology: A unifying triple network model. *Trends Cogn. Sci.* **15**, 483–506 (2011).
38. S. Hong *et al.*, Complement and microglia mediate early synapse loss in Alzheimer mouse models. *Science* **352**, 712–716 (2016).
39. E. Sharp *et al.*, Synaptic density is associated with cognitive performance in early Alzheimer's disease: A PET imaging study with [11C]UCB-J. *Am. J. Geriatr. Psychiatry* **29**, S119–S120 (2021).
40. J. A. Avery *et al.*, Major depressive disorder is associated with abnormal interoceptive activity and functional connectivity in the insula. *Biol. Psychiatry* **76**, 258–266 (2014).
41. J. D. Bremner *et al.*, Reduced volume of orbitofrontal cortex in major depression. *Biol. Psychiatry* **51**, 273–279 (2002).
42. L. Schmaal *et al.*, Cortical abnormalities in adults and adolescents with major depression based on brain scans from 20 cohorts worldwide in the ENIGMA Major Depressive Disorder Working Group. *Mol. Psychiatry* **22**, 900–909 (2017).
43. T. G. C. Dias *et al.*, Reward circuit connectivity relates to delay discounting in children with attention-deficit/hyperactivity disorder. *Eur. Neuropsychopharmacol.* **23**, 33–45 (2013).
44. M. Yu *et al.*, Childhood trauma history is linked to abnormal brain connectivity in major depression. *Proc. Natl. Acad. Sci.* **116**, 8582–8590 (2019).
45. Y. Zhang *et al.*, Dysfunction in sensorimotor and default mode networks in major depressive disorder with insights from global brain connectivity. *Nat. Ment. Health* **2**, 1371–1381 (2024).
46. J. Yuan *et al.*, Altered spontaneous brain activity in major depressive disorder: An activation likelihood estimation meta-analysis. *J. Affect. Disord.* **314**, 19–26 (2022).
47. B. Yu, X. Sun, M. Xia, White matter functional connectome gradient dysfunction in major depressive disorder. *Psychoradiology* **5**, kkaf008 (2025).
48. X. Liang *et al.*, Dissecting human cortical similarity networks across the lifespan. *Neuron* **113**, 3275–3295.e3211 (2025).
49. E. Richard *et al.*, Late-life depression, mild cognitive impairment, and dementia. *JAMA Neurol.* **70**, 383–389 (2013).
50. L. L. Beason-Held *et al.*, Changes in brain function occur years before the onset of cognitive impairment. *J. Neurosci.* **33**, 18008–18014 (2013).
51. J. Straub *et al.*, Adolescent depression and brain development: Evidence from voxel-based morphometry. *J. Psychiatry Neurosci.* **44**, 237–245 (2019).
52. S. M. Szymkowicz, A. R. Gerlach, D. Homiack, W. D. Taylor, Biological factors influencing depression in later life: Role of aging processes and treatment implications. *Transl. Psychiatry* **13**, 160 (2023).
53. P. R. Goldin, K. McRae, W. Ramel, J. J. Gross, The neural bases of emotion regulation: Reappraisal and suppression of negative emotion. *Biol. Psychiatry* **63**, 577–586 (2008).
54. S. Grimm *et al.*, Imbalance between left and right dorsolateral prefrontal cortex in major depression is linked to negative emotional judgment: An fMRI study in severe major depressive disorder. *Biol. Psychiatry* **63**, 369–376 (2008).
55. S. Wada *et al.*, Volume of the right supramarginal gyrus is associated with a maintenance of emotion recognition ability. *PLoS One* **16**, e0254623 (2021).
56. G. Silani, C. Lamm, C. C. Ruff, T. Singer, Right supramarginal gyrus is crucial to overcome emotional egocentricity bias in social judgments. *J. Neurosci.* **33**, 15466–15476 (2013).
57. M. L. Perlis, D. E. Giles, W. B. Mendelson, R. R. Bootzin, J. K. Wyatt, Psychophysiological insomnia: The behavioural model and a neurocognitive perspective. *J. Sleep Res.* **6**, 179–188 (1997).
58. W. D. Killgore, Z. J. Schwab, M. Kipman, S. R. DelDonno, M. Weber, Insomnia-related complaints correlate with functional connectivity between sensory–motor regions. *Neuroreport* **24**, 233–240 (2013).
59. V. A. Kulkarni, B. L. Firestein, The dendritic tree and brain disorders. *Mol. Cell. Neurosci.* **50**, 10–20 (2012).
60. A. Soetanto *et al.*, Association of anxiety and depression with microtubule-associated protein 2- and synaptopodin-immunolabeled dendrite and spine densities in hippocampal CA3 of older humans. *Arch. Gen. Psychiatry* **67**, 448–457 (2010).
61. R. S. Duman, G. K. Aghajanian, Synaptic dysfunction in depression: Potential therapeutic targets. *Science* **338**, 68–72 (2012).
62. D. A. Tata, B. J. Anderson, The effects of chronic glucocorticoid exposure on dendritic length, synapse numbers and glial volume in animal models: Implications for hippocampal volume reductions in depression. *Physiol. Behav.* **99**, 186–193 (2010).
63. J. Eckmann, S. H. Eckert, K. Leuner, W. E. Muller, G. P. Eckert, Mitochondria: Mitochondrial membranes in brain ageing and neurodegeneration. *Int. J. Biochem. Cell Biol.* **45**, 76–80 (2013).
64. W. E. Müller, A. Eckert, C. Kurz, G. P. Eckert, K. Leuner, Mitochondrial dysfunction: Common final pathway in brain aging and Alzheimer's disease–therapeutic aspects. *Mol. Neurobiol.* **41**, 159–171 (2010).
65. J. J. Chen, B. P. Yu, Alterations in mitochondrial membrane fluidity by lipid peroxidation products. *Free Radic. Biol. Med.* **17**, 411–418 (1994).
66. H. Wang, S. Lautrup, D. Caponio, J. Zhang, E. F. Fang, DNA damage-induced neurodegeneration in accelerated ageing and Alzheimer's disease. *Int. J. Mol. Sci.* **22**, 6748 (2021).
67. M. Tran, P. H. Reddy, Defective autophagy and mitophagy in aging and Alzheimer's disease. *Front. Neurosci.* **14**, 612757 (2020).
68. Q. Cai, Y. Y. Jeong, Mitophagy in Alzheimer's disease and other age-related neurodegenerative diseases. *Cells* **9**, 150 (2020).
69. T. Paus *et al.*, Maturation of white matter in the human brain: A review of magnetic resonance studies. *Brain Res. Bull.* **54**, 255–266 (2001).
70. J. Pujol *et al.*, Delayed myelination in children with developmental delay detected by volumetric MRI. *Neuroimage* **22**, 897–903 (2004).
71. C. R. Chin Fatt *et al.*, Effect of intrinsic patterns of functional brain connectivity in moderating antidepressant treatment response in major depression. *Am. J. Psychiatry* **177**, 143–154 (2020).
72. P. Kochunov *et al.*, Functional vs structural cortical deficit pattern biomarkers for major depressive disorder. *JAMA Psychiatr.* **82**, 582–590 (2025).
73. C.-G. Yan *et al.*, Reduced default mode network functional connectivity in patients with recurrent major depressive disorder. *Proc. Natl. Acad. Sci.* **116**, 9078–9083 (2019).
74. C. Pang, topography_MDD repository. GitHub. https://github.com/ALICE1029/topography_MDD. Deposited 14 February 2026.
75. Z. Cui *et al.*, Individual variation in functional topography of association networks in youth. *Neuron* **106**, 340–353.e348 (2020).
76. M. Yu *et al.*, Statistical harmonization corrects site effects in functional connectivity measurements from multi-site fMRI data. *Hum. Brain Mapp.* **39**, 4213–4227 (2018).
77. A. Eklund, T. E. Nichols, H. Knutsson, Cluster failure: Why fMRI inferences for spatial extent have inflated false-positive rates. *Proc. Natl. Acad. Sci.* **113**, 7900–7905 (2016).
78. R. A. Rigby, D. M. Stasinopoulos, Using the box-cox t distribution in GAMLSS to model skewness and kurtosis. *Stat. Model.* **6**, 209–229 (2006).
79. M. A. Di Biase *et al.*, Mapping human brain charts cross-sectionally and longitudinally. *Proc. Natl. Acad. Sci.* **120**, e2216798120 (2023).
80. J. B. Burt, M. Helmer, M. Shinn, A. Anticevic, J. D. Murray, Generative modeling of brain maps with spatial autocorrelation. *Neuroimage* **220**, 117038 (2020).
81. Y. Zhou *et al.*, Metascape provides a biologist-oriented resource for the analysis of systems-level datasets. *Nat. Commun.* **10**, 1523 (2019).